# Quantitative Phase Velocimetry for Label-Free Measurement of Intracellular Mass Transport Velocity

Soorya Pradeep[1], Thomas A. Zangle[1,2]*

[1] Department of Chemical Engineering, University of Utah, Salt Lake City, UT 84112, USA

[2] Huntsman Cancer Institute, University of Utah, Salt Lake City, UT 84112, USA

*Corresponding author. Email tzangle@chemeng.utah.edu

## ABSTRACT

Transport of mass within cells helps maintain homeostasis and is disrupted by disease and stress. Here, we develop quantitative phase velocimetry (QPV) as a label-free approach to make the invisible flow of mass within cells visible and quantifiable. We benchmark our approach against alternative image registration methods, a theoretical error model, and synthetic data. Our method tracks not just individual labeled particles or molecules, but the entire flow of material through the cell. This enables us to measure diffusivity within distinct cell compartments using a single approach, which we use here for direct comparison of nuclear and cytoplasmic diffusivity. As a label-free method, QPV can be used for long-term tracking to capture dynamics through the cell cycle. Finally, based on the known effective particle size, we show that QPV is an accessible method to measure intracellular viscosity.

## INTRODUCTION

Orderly transport is essential for cell function and growth. To maintain homeostasis, cells continuously transport materials, including nutrients from the surrounding environment (*1*), ions through cell membranes (*1*), and liquids (*2*) and structural polymers into cell podia to drive cell motion (*3*). In turn, cell transport can be impacted by disease (*4*) and stress (*5, 6*). Measurement of transport within cells can therefore improve our understanding of cell behavior, disease, responses to environmental stresses and potential disease therapies. Most studies conclude that transport in cells is diffusive and contributed by boundary forces due to the deformation and movement of cells (*7*). However, more recent work has shown that motion in the bulk of the cell is not just diffusive but has advective components (*8*).

Fluorescent markers are the most commonly used tools to study transport within cells as they provide distinct signals with low background, making them easy to track. Fluorescence can be used to track entire cells (*9*), intracellular organelles (*10*), or one or more specific molecular components (*11-13*). For example, tracking fluorescently labeled organelles with multiple-particle tracking enabled the measurement of cytoplasmic flow pattern driven by cell boundary deformations (*7*). Measurement of flow of fluorescently tagged intercellular actin was used to quantify the pressure and forces inside the cell (*14*) and actin polymerization rates (*15*). Confocal fluorescence imaging has also been used at a higher resolution to study nuclear dynamics, structure, and organization (*16*). Movement patterns of actin on myosin and microtubules have also been studied both *in vitro* and *in vivo* using fluorescent markers (*12, 17*). Despite the wide use of fluorescent markers in transport studies, the use of fluorescence come with the disadvantages of photobleaching, which limits the time over which transport can be tracked, and phototoxicity, which induce stress and modifies cell behavior (*18, 19*). The number of components in cells which can be labelled at a time is also limited (*20*) and fluorescence also cannot calculate the velocities in the untagged regions.

Label-free techniques use no markers and thus avoid many of the issues associated with fluorescence. Label-free methods include phase-contrast imaging, differential interference contrast (DIC), Raman microscopy, and quantitative phase imaging (QPI). These imaging methods have been widely used to track the dynamics of whole cell motion (*21-26*). Comparatively less work has applied label-free methods to measure transport within individual

cells. For example, one study on high-resolution DIC microscopy revealed the movement dynamics of single vesicles found on cell membranes in different conditions of cell (*27*), while another has applied DIC to segment and track the centroid of vesicles within a cell (*28*). Raman microscopy has been applied to track smaller components such as lipid droplets (*29*).

Quantitative phase imaging (QPI) is a label free imaging technique which measures the phase shift that occurs as light passes through a material with higher refractive index (*30*). The phase shift measured with QPI is directly proportional to the dry mass content in the sample (*31*). There are multiple methods available for QPI, including digital holography (*32*), spatial light interference (*33*), differential phase contrast (*34*), or wavefront sensing (*35, 36*). Other label-free methods like DIC show contrast due to phase gradients in just a single orientation, and phase-contrast images contain halos that make quantitative analysis difficult (*21*). QPI is, therefore, a good candidate for studying transport within cells due providing quantitative data without artifacts.

Previous work with QPI has used the contrast produced by localized variation in biomass density to track well-defined sub-cellular components as well as the average rate of mass motion. QPI based on interferometry has been used early as 1989 to measure the overall patterns of dry mass flux in fibroblast cells with low spatial and temporal resolutions (*37*) as well as the motion of mass due to induced deformations with magnetic beads (*38*). QPI images of neurons have been used to manually track individually identified vesicles transporting cargo along dendrites to characterize their motion as active diffusion (*39*). In terms of average transport velocities, the rate of bulk motion within stem cells during differentiation was characterized from the temporal autocorrelation of QPI data (*40*), a quantity later linked to cell rheological properties (*41*). Disorder strength from spatial variance in QPI phase has also been used to estimate rheological property of cells (*42*). The Laplace transform of QPI images has been applied to measure the overall diffusion rate of organelles and vesicles in neuron and cardiomyocytes (*43*). Average mitochondrial network dynamics and lipid droplet flux have also been characterized using 3D refractive index maps obtained using tomographic QPI (*44*). Work using dispersion phase microscopy and phase correlation imaging developed using QPI has looked at localized dynamics (*45*) and overall cell dynamics (*46*). However, although QPI provides data on the redistribution of mass with cells, this approach has not been applied for continuously tracking all

subcellular regions inside cells in an automated fashion or to measure mass transport velocity fields.

Due to the lack of prominent features in label-free images, tracking velocity vectors from label-free data typically requires segmentation of well-defined features within cells or tissues. Transport velocities can then be measured by tracking individually identified organelles or other structures from frame to frame. In contrast, automated velocimetry can be performed on all regions of cells even without well-defined structures amenable to segmentation. Automated image velocimetry, which computes velocities using feature registration, is well-established with fluorescence images or for tracking beads. Image velocimetry automates velocity measurements, reducing processing time and helps visualize the overall flow structure. For example, studies on actin bulk flow and structural organization in cells has been made possible by image velocimetry techniques, combined with sparse fluorescent labeling of actin monomers (*15*). However, aside from measuring the rotation (*44*) and motion of cell nuclei (*47*), relatively few works have used automated label-free velocimetry to measure intracellular transport.

Some common particle image velocimetry (PIV) image registration methods are optical flow reconstruction (OFR) (*15*), mutual information (MI) (*48*), normalized cross-correlation (NCC) (*49*), and sum of squared differences (SSD) (*50*). For example, velocity fields in migrating epithelial cells imaged using phase contrast have been measured using cross-correlation (*51*). Diffusion in lipid membranes was measured using cross-correlation with a combination of fluorescence and total internal reflection images (*52*). Other methods like MI and feature matching using least squares regression on Hough transformed data (*53*) have also been applied to biological images and for feature registration on high-resolution CT scans (*48*). SSD has been shown to have increased accuracy and lower computation time than MI for medical image registration (*54*) as well as a lower computational cost than NCC for template matching (*50*).

In this work we combine the benefits of both automated image velocimetry and label-free QPI to develop an approach we call quantitative phase velocimetry (QPV). We find that the SSD image registration technique has superior performance when applied to QPI data. To understand the sources of error in QPV, we also developed a theoretical model that matches experimental results. We then apply our QPV technique to measure dry mass transport inside cells. With this data, we quantify the velocity distribution in the nuclear and cytoplasmic regions of cells to study

cell deformation patterns. We also show the use of QPV for mean square displacement (MSD) analysis to analyze variation in the effective diffusivity of dry mass in the nucleus and cytoplasm of cells during different phases of the cell cycle. Finally, we extend this measurement to quantify intracellular viscosity.

## RESULTS

### 1. Development of QPV from QPI data

We developed QPV to measure intracellular dry mass velocity from QPI data (**figure 1**). We capture QPI data using an inverted microscope with a quadri-wave lateral shearing interferometry wavefront sensing camera (*55*) (**figure 1a**) to obtain images of cell mass distributions over time. The resulting images of cell mass distribution show both large and small-scale structures within cells that can serve as features for velocimetry. For example, individual retinal pigment epithelial (RPE) cells show higher mass density in the nucleus and center of the cell and lower mass in the cell podia, as well as smaller scale mass puncta (**figure 1b**). Taking the difference between QPI images over time illustrates the movement of mass captured by QPI (**figure 1c)**. In this difference image showing 10 minutes of motion, blue regions indicating loss of mass are predominantly on the right side of the image, while red regions showing an increase in mass are predominantly on the left. This indicates an overall movement of the cell dry mass from the top right corner to the bottom left corner of the image frame. QPV uses these data to measure the movement of mass using the principles of PIV. As expected in this individual, example cell, the distribution of intracellular dry mass velocity determined by QPV shows dry mass velocity vectors pointing from the top right to the left bottom of the frame, as well as localized deviation from that overall trend (**figure 1d**).

Our implementation of QPV is based on the SSD image registration method (*50*) to track the transport of mass within cells from unlabeled QPI images. We applied the SSD calculation to 15 by 15 pixel (3.57 by 3.57 μm) interrogation windows within cells. A magnified view of one 15 by 15 pixels interrogation window inside an example cell difference image (**figure 1c**) shows the movement of individual cell components from the position indicated by a red arrow to a position on the left side of the window indicated by a black arrow (15 by 15 pixel inset in **figure 1c)**. SSD produces the lowest sum of squared difference when such patterns of mass within an interrogation window overlap between two displaced windows from successive imaging frames. As expected, in the example shown in **figure 1c**, the SSD computed for the specified 15 by 15 pixel interrogation window has a lowest value at a displacement corresponding to the motion of features within this region (**figure S1a)**. We implemented Gaussian fitting on the 3 by 3 pixel region neighborhood around the lowest value of the computed SSD for sub-pixel localization of

displacements (**figure S1b)**. This results in the measured displacements that form the basis of QPV (**figure S1c**). From the known time gap between frames set during cell imaging, we compute the velocity of mass transport from these displacement measurements (**figure 1d**).

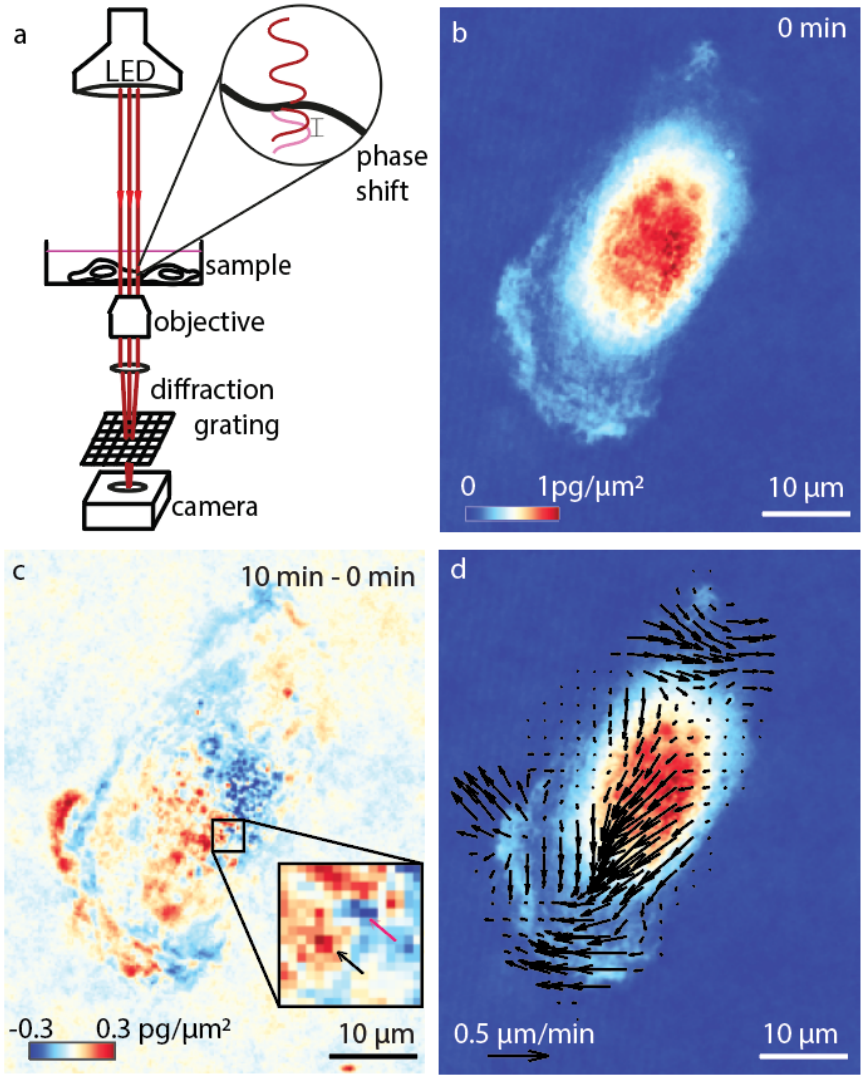


**Figure 1. Quantitative phase velocimetry (QPV) measures intracellular dry mass movement.** (a) Quantitative phase imaging (QPI) measures the phase shift of light passing through a cell, which is used to compute the dry mass distribution in cells over time. (b) Dry mass distribution in RPE cell imaged at 120X magnification, at $t = 0$ min. The scalebar indicates 10 μm length. (c) The difference in QPI mass distribution of the RPE cell in (b) from an image taken at $t$ = 10 min later minus the image at 0 min reveals cell motion. The color scale shows the net displaced mass over this interval (red increase, blue decrease). The inset in (c) shows a 15x15 pixel interrogation window that illustrates the change in position of an individual subcellular feature from the position marked with a red arrow to the position marked with a black arrow (d) The resulting intracellular biomass velocity field computed using quantitative phase velocimetry (QPV). Velocity magnitude indicated with a 0.5 μm/min scalebar.

Next, we tested the performance of SSD relative to several image registration methods commonly used for PIV: normalized cross-correlation (NCC), optical flow reconstruction (OFR), and mutual information (MI). With each method, we estimated the resolution and accuracy of velocity measurement on fixed RPE and MCF7 cells moving at known velocity as a velocity standard with the same distribution of intracellular features as in living cells (**figure 2** and **figure S2**). We imaged fixed RPE cells and fixed MCF7 cells moved artificially using the microscope stage at a step size of 0.05 μm between each frame, representing 22% of a pixel in the specimen plane to enable evaluation of sub-pixel resolution. As expected, the displacement distribution computed by SSD of example fixed cells after a total of 1.5 μm downward stage motion shows uniform displacement distribution in all interrogation windows pointing in the direction of stage motion (**figure 2a** and **figure S2a**).

The performance of image registration methods with a given dataset depends critically on the distribution of spatial features and noise in the data. To study the impact of these features on QPV, we generated two types of simulated data, one set with uniform circles (**figure 2b** top middle) and the other with non-uniform-sized circles (**figure 2b** top right). Perlin noise was added to the images to match the continuous local variation background noise in our QPI data (**figure 2b** bottom middle and bottom right), reducing the magnitude of the power spectral density (**figure S2b**). Perlin noise was chosen based on a close match to the power spectrum of background noise in QPI images. To understand the distribution of spatial features in the image, we computed the power spectrum of 120X magnification RPE QPI image and MCF7 QPI image and compared it with simulated data (**figure 2c** and **figure S2b**). The power spectrum of the uniform-sized circle data shows narrow ranges of spatial frequencies characterized by the size of the beads and the space between them while the non-uniform circles have a smoother power spectrum reflecting the presence of a wider range of spatial frequencies (**figure S2b**). The power spectra of the RPE fixed cell, MCF7 fixed cell, and polystyrene beads imaged at 20X magnification match best with the power spectrum of non-uniform synthetic data with noise (**figure 2b-c** and **figure S2b**). Therefore, based on the power spectrum analysis, non-uniform spatial features with added low spatial frequency noise are suitable synthetic data for testing which image registration method works best with QPI data.

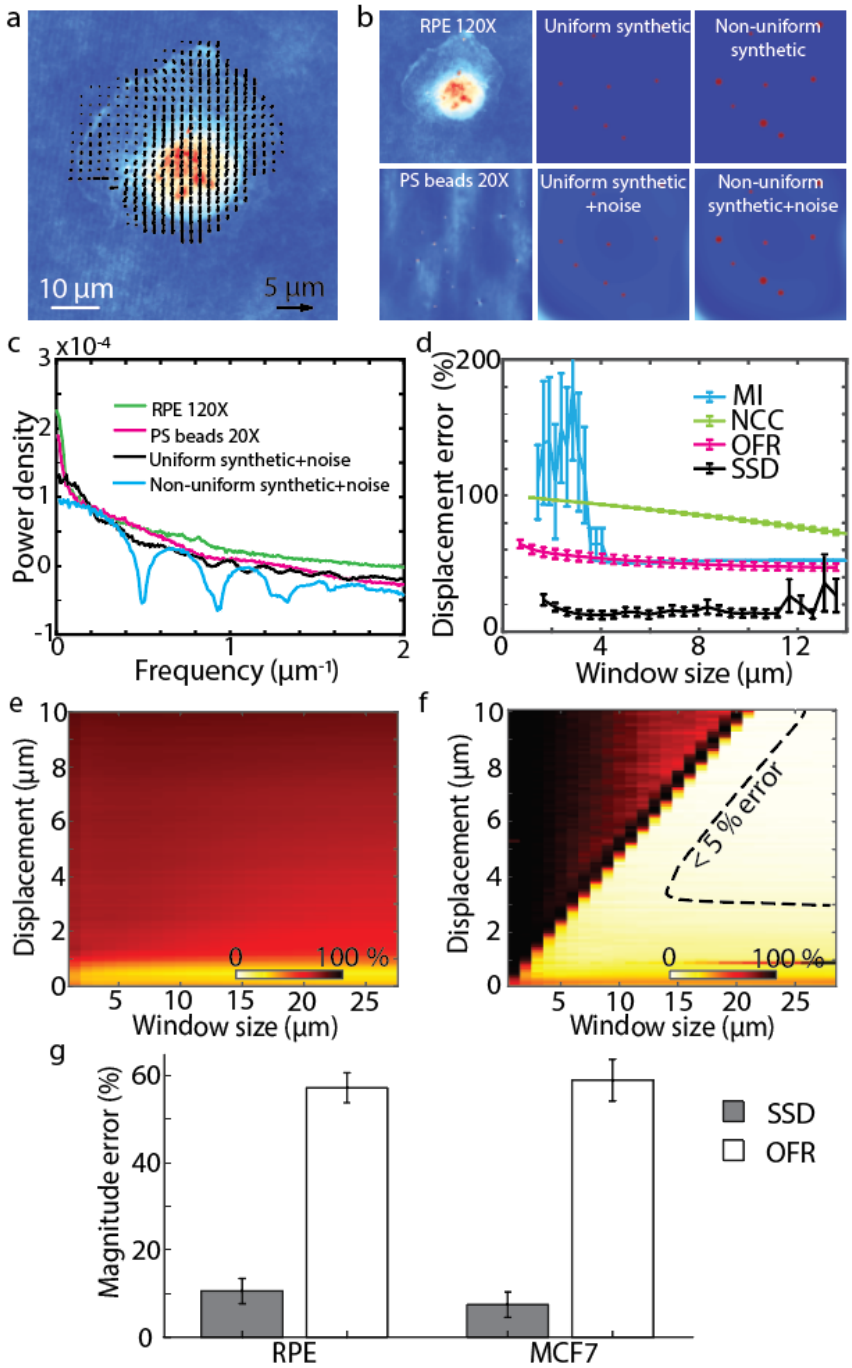


**Figure 2. SSD image registration measures intracellular velocity from QPI data with higher accuracy than OFR, MI and NCC.** (a) QPV on RPE fixed cell measures the intracellular displacement during microscope stage translation. (b) Comparison of background corrected QPI image of RPE fixed cell at 120 X (top left) and polystyrene beads at 20X (bottom left) to synthetically generated uniform and non-uniform circle data, with added Perlin noise (top middle and right) and without added Perlin noise (bottom middle and right) (c) Power spectrum of the QPI data (green and magenta) and synthetic data with noise (black) in (b) shows the similarity of QPI data to the non-uniform circle synthetic data. (d) Comparison of mutual information (MI), normalized cross correlation (NCC), optical flow reconstruction

(OFR) and sum of squared difference (SSD) for intracellular velocity computation on QPI data at different interrogation window sizes shows SSD has highest accuracy at small window sizes ($n$ = 11, error bar shows standard error of the mean, SEM). (e) Velocity accuracy versus both interrogation window size and displacements of RPE fixed cell using OFR shows that OFR is limited to measuring a very narrow range of displacements with acceptable accuracy ($n$ = 11). Yellow/white – high accuracy, red-black – low accuracy. (f) QPV velocity measurement accuracy versus interrogation window size and displacements of fixed RPE cells show typically less than 10% error when the interrogation window size is smaller than the displacement to be measured with a region of less than 5% error indicated as a dashed line ($n$ = 11). (g) Displacement magnitude error for 15 x 15 pixel interrogation window size averaged over $n$ = 11 RPE and $n$ = 9 MCF7 cells, computed with SSD and OFR methods. Error bars show standard error of the mean.

The window size used for estimating displacements determines the spatial resolution of our velocimetry approach. The smaller the window size, the higher the spatial resolution of the resulting velocity field. Therefore, we computed the measurement accuracy of 0.1 µm (0.42 x a single pixel) displacements of fixed cells and synthetic data using each method with interrogation window sizes ranging from 5 to 59 pixels (1.19 µm to 14 µm) square. This displacement error is the key determinant of the error in computed velocity as the time between frames is tightly controlled during imaging. Of the four methods tested, SSD performed best overall, with error below 10% at the smallest window sizes and a large region of less than 5% error (**figure 2d** and **figure S2b**). MI and NCC work moderately well with large windows, however, they show inferior performance at small window sizes with MI in particular showing highly variable errors for small displacements (**figure 2d** and **figure S2b)**. NCC also had poor performance with synthetic data (**figure S3a**). SSD and OFR performed well for both uniform and non-uniform synthetic data down to for window sizes above 2 µm (**figure S3b-c**).

The image registration method used for QPV should perform well over a wide range of displacements as cells typically display a wide range of motion from sub-pixel movement in the nucleus to highly deforming multiple pixel displacements in the podia regions of the cytoplasm. Based on their performance at small window sizes and with synthetic data, we further measured displacement error with SSD and OFR for displacements from 0.1 to 10 µm and interrogation window sizes from 1 to 14 µm. The results for OFR with fixed RPE cells shows greater than 50% error for displacement measurements above 1 µm at all interrogation window sizes tested (**figure 2e**). The same was seen with fixed MCF7 cells (**figure S4a**). Performance of OFR at large displacements can be improved using Gaussian blurring (*56*). In application to QPI data,

we found that a displacement of 1.75 µm of RPE and MCF7 fixed cell can be measured accurately by blurring the image with a Gaussian filter with a standard deviation of 2.1 µm (9 pixels) or higher (**figure S4c** and **figure S4d**) at low interrogation window size. The reproduction of OFR error for varying displacements with a MCF7 fixed cell with 1.2 µm Gaussian blur for the same range of displacements as **figure S4a** shows a slight increase in the range of displacements measured with error below 20% (**figure S4b**). However, Gaussian blurring comes at the cost of losing the ability to resolve small-scale differences in deformation within cells. On the other hand, SSD gives an error of less than 10% for any displacement, as long as the window size for the calculation is at least as large as the displacement itself and less than 5% for a subset of this region (**figure 2f**). The overall error for measuring a 1.05 µm displacement at a 3.6 µm window size with SSD is below 10% for both RPE and MCF7 cells but above 50% with OFR (**figure 2g**). We also evaluated error in displacement direction measurement. We found that SSD measures direction with less than 10º error at window sizes equal to or greater than the measured displacement for RPE and MCF7 fixed cells and less than 5º for a narrower region (**figure S5b** and **figure S5d**), whereas the average OFR direction measurement accuracy is around 30º (**figure S5a** and **figure S5c**). Therefore, considering accuracy, spatial resolution and the ability to measure a wide range of displacements, we chose SSD as the image registration method for QPV.

## 2. Theoretical modelling of displacement measurement accuracy

To understand the source of errors in QPV, we developed a model that account for key parameters that contribute to measurement noise. These are: the size range of cell features which impacts Brownian diffusion of cell components and the ability to visualize displacement with the interrogation window size chosen, the interrogation window size which determines the maximum measurable displacement, and the optical resolution limit of the microscope. In contrast to uniform-sized features, such as those generated for testing with synthetic data, power spectra of typical QPI cell data show a continuous decay, indicating a wide variation in cell feature size used for velocimetry (**figure 2c**). Converting frequency to equivalent particle size shows that the features potentially tracked by QPV range in size from organelle-size puncta of mass to the entire cell (**figure 3a-b**). One source of error is that QPV cannot measure the displacement of particles larger than the interrogation window size. This is illustrated by the two planes showing

the displacement magnitude error for two particle sizes, 2 and 30 µm, in an RPE cell, with increased error for larger particle sizes (**figure 3c**). Additionally, if the displacement is greater than the window size used, the estimated displacement will be incorrect. This is reflected as a region of very large error for large displacements and small window sizes (**figure 3c**). Finally, displacements below the optical resolution of the imaging system are also assumed not to be measurable. This is reflected by a narrow range of high predicted errors for displacement below 0.48 µm at the bottom of the averaged chart, based on the Abbe's criterion for diffraction limited resolution (**figure 3c**).

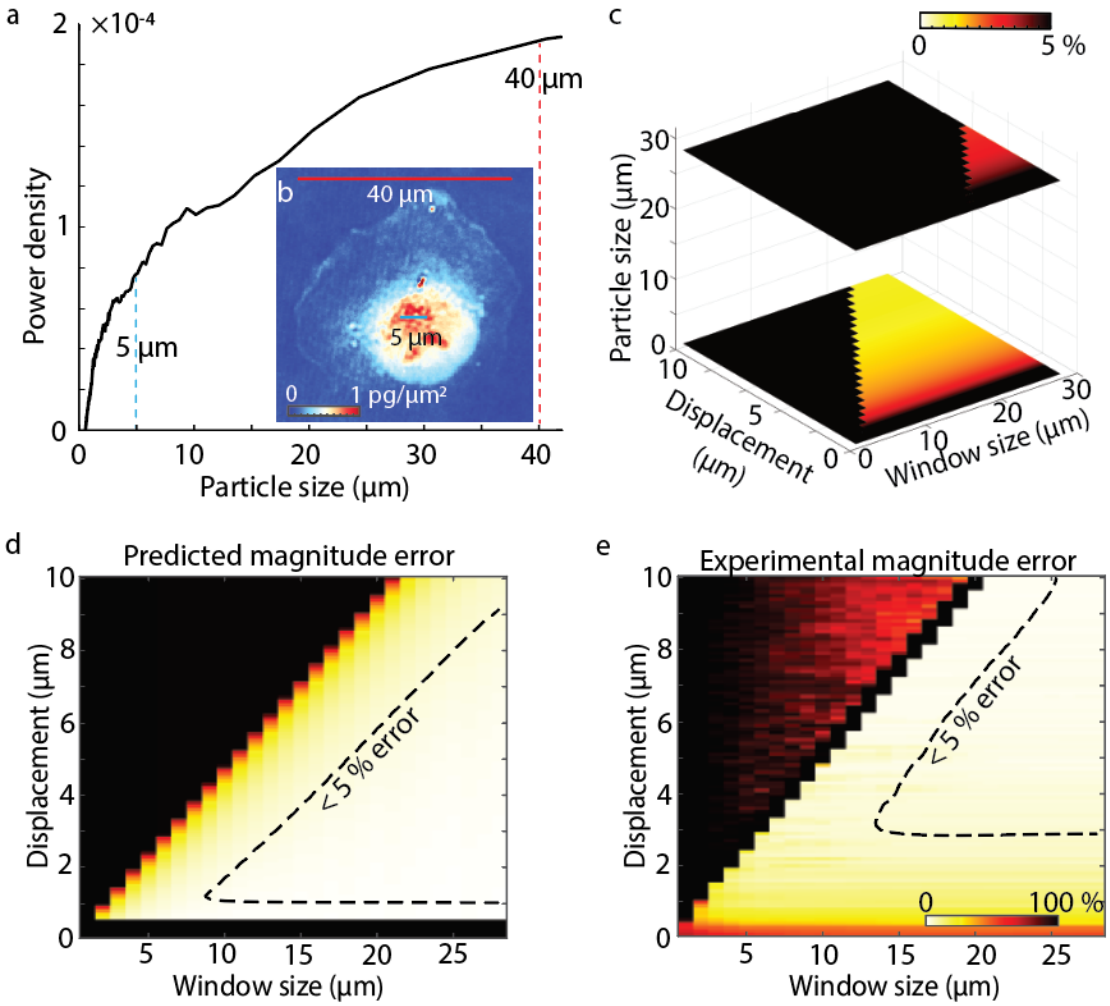


**Figure 3. Modelled QPV displacement measurement error agrees with experimental measurements**. (a) 2 µm organelle structure inside 40 µm RPE fixed cell illustrating the range of features captured by QPI. Scale bars show 5 µm (blue) and 40 µm (red). Colormap shows dry mass density in pg/µm$^2$. (b) Power spectral density versus effective particle size of RPE fixed cells ($n$ = 3). Power spectral density corresponding to both 5 µm and 40 µm structures is indicated. (c) Theoretical displacement estimation error at 2 and 30 µm particle size for all

tested displacements and window sizes. (d) Averaging the size dependent model results as in (c), weighted by the actual distribution of particle sizes (a) gives a predicted error which is in agreement with the (e) measured error from the matched RPE cell using experimental data. Colormaps in (d) and (e) are the same.

To account for the range of feature sizes captured by QPI and their individual contributions to measurement error, we compute the theoretical error for all particle sizes in a cell up to 40 μm, the size of a whole cell (**figure 3c**, **figure S6c-d**), then perform a weighted average of these particle errors based on the power spectrum for the cell (**figure 3b**, **figure S6b**). The resulting prediction of the error in displacement magnitude (**figure 3d**, **figure S6e**) are in good agreement with the experimentally computed error for both RPE (**figure 3e** and MCF7 cells (**figure S6f**). In addition, we observe reasonable agreement in the predicted and measured displacement direction error (**figure S7**). Application of this model and validation allows us to predict the minimum window size for accurate intracellular velocimetry. For example, for RPE and MCF7 cells imaged at 120X magnification every 1 minute, the typical observed range of displacement varies from 0 to 5 pixels outside of the very fast moving podia. Therefore, we use a 15 by 15 pixel interrogation window, which corresponds to an area of 12.75 $\mu m^2$.

### 3. Application of QPV for measurement of intracellular displacements

QPV tracks both overall cellular deformation as well as the motion of individual regions within cells. As a method based on QPI, which measures dry mass distributions (*31*), QPV measures displacement of dry mass. Sample results for an RPE cell are shown in **figure 4**. The deformation of a uniform grid overlayed on the RPE cell image from time 0 minutes (**figure 4a**) to 30 minutes (**figure 4b**) shows compression of the grid points in the nuclear region and the spacing out of points in the podia region (**figure 4b**), reflecting the observed compression of the cell as its podia move upward within the image frame (**movie S1**). Each square enclosed by four grid points in **figure 4a** represents a volume encompassing a specific quantity of dry mass in the cell. Using QPV, we track each region of dry mass as it moves and deform with time. The motion of five such volumes in the nuclear and cytoplasmic regions of the indicated RPE cell shows upward movement of the control volumes and the movement of the cell over 30 minutes (**figure 4c-d** and **movie S2**). From these tracks, we can see that mass originating from the central region of the cell are more direction oriented with smaller scale fluctuations than mass originating in the lower density regions of the cytoplasm.

QPV data quantifies the overall velocity of each region within the cell. The mean velocity distribution over 30 minutes in the cell shows a higher average velocity in the cytoplasm region, with a moderate velocity in the nuclear region (**figure S8a**). To more systematically assess differences between the cytoplasm and nucleus, we segmented the nuclear region from the cytoplasm of the RPE cell using the fluorescent images of an expressed FUCCI marker (*57*). Separating the velocities in the nucleus and cytoplasm and comparing them to the cell centroid velocity showed no difference as the cell nucleus and bulk of the cytoplasm moves with the cell ($n$ = 59 cells, **figure S8b**). We compute the deformation velocity as the velocity of the volumes inside the nucleus and cytoplasm relative to the cell centroid velocity. The deformation velocity map overlayed on the RPE cell (**figure 4e**), shows a similar distribution as the overall distribution of intracellular velocities **(figure S8a**). However, the velocity magnitude in the regions showing the smallest deformations, such as the nucleus, are reduced to around zero (**figure 4e**). The average deformation velocity from the nucleus and cytoplasm of the cell also reflects a larger deformation in the cytoplasm compared to the cell nucleus ($n$ = 59 cells, **figure 4f**). Thus, the nuclei of RPE cells move more in line with the overall cell body relative to the cytoplasm, with the podia in particular exhibiting a larger velocity relative to that of the whole cell.

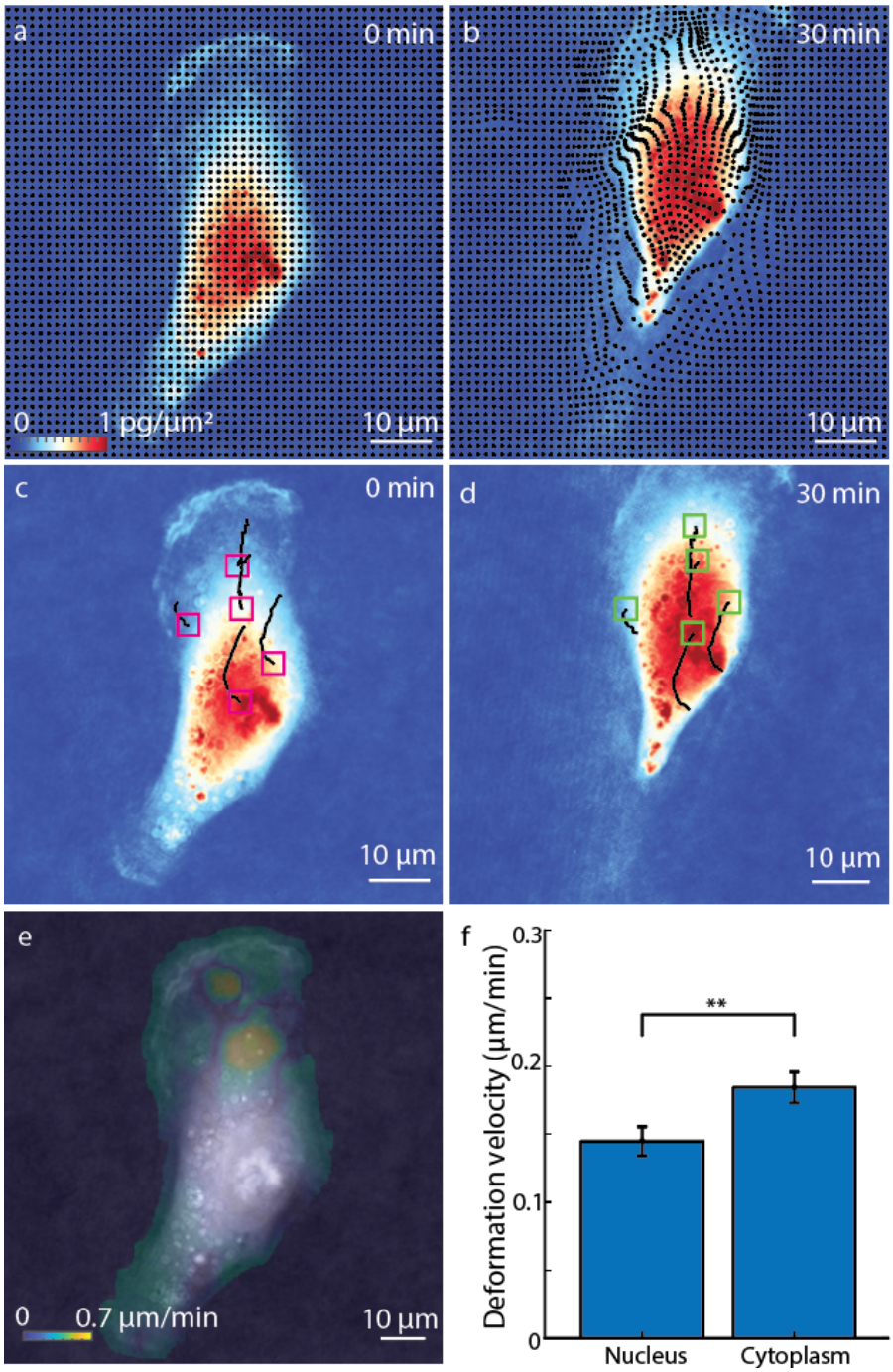


**Figure 4. QPV shows spatial and temporal dynamics of biomass motion within cells.** (a) Grid markers depict 4 by 4 pixel intracellular volume centroids overlayed on an RPE cell at 120 X magnification (b) which deforms from (a) to (b) due to movement of the cells in 30 minutes. (c) Dry mass inside control volumes initial positions marked using magenta boxes travel along the black line to reach the final positions indicated using green boxes in (d) in 30 minutes. (e) Deformation velocity, the whole cell velocity subtracted intracellular velocity distribution of dry mass, inside the RPE cell (f) Deformation velocity of dry mass in nucleus and cytoplasm of RPE cells, shows higher deformation in cytoplasm than nucleus ($n$ = 59, error bars show standard error of the mean). ** $p < 0.01$.

## 4. Decreasing intracellular diffusion with cell cycle progression

The subcellular distribution of diffusivity has been used to understand the dependence of cell functions on intracellular physical properties, for example, the distribution of transcription activity inside the nucleus relative to heterochromatin packing (*16*) and organization of the cytoplasm. However, most previous studies measuring diffusion in cells uses fluorescent markers, typically limiting the measurement time period to periods as short as just a few minutes (*16*). Such work cannot quantify changes in the transport characteristics continuously over a longer period, ex. several hours, while intermittently imaging random cells at different time points (*58*) cannot track the characteristics of a group of selected cells over time. Using QPV, we tracked the intracellular dynamics of mass within every control volume within the cell (**Figure 4c-d**) to measure transport of mass continuously for eight hours while simultaneously monitoring cell cycle progression with the FUCCI cell cycle indicator (*57*).

We measured the mean squared displacement (MSD) of the deformation, or displacement relative to cell centroid displacement, of all tracked intracellular mass from QPV of RPE cells (**figure 5**). The slope and intercept of the MSD plot was used to measure the anomalous constant and diffusion coefficient, respectively, of each intracellular region tracked with QPV (**figure 5a-c**). To validate our MSD calculation, we compare the anomalous and diffusion constants of live RPE cells to fixed cells moved artificially on a stage. As expected, these results show an average diffusion coefficient of live cells was 40 times more than the fixed cells (**figure S9a**) with a significantly reduced, sub-diffusive anomalous constant (**figure S9b**). A map of anomalous constant and diffusion coefficient in the RPE cell from **figure 5a** shows that most of the volumes inside the cell, including volumes in the nucleus and cytoplasm, exhibit anomalous to normal diffusion (**figure 5b** and **5c** respectively). Nuclear boundaries were determined by alignment to fluorescence images of FUCCI cell cycle markers (**figure S10**). Some volumes in the peripheral podia region of the cell exhibit more active diffusion. Overall, we found that QPI-tracked biomass exhibits moderately sub-diffusive, anomalous diffusion (**figure S9b**).

Consistent with deformation magnitude results (**figure 4**), the cytoplasm exhibits an overall larger range of MSD than the nucleus (**figure 5d-e**). The diffusion coefficient in the nucleus was slightly higher than in the cytoplasm (**figure S11a**). However, the anomalous constant in the nucleus and cytoplasm of live cells did not show any significant difference ($n$ = 119, **figure**

**S11b**). To understand if this difference is the result of variation during specific cell cycle phases, we used the FUCCI cell cycle marker to categorize individual cells as G1, S, or G2 (**figure 5f**). These data indicate that, during S-phase, the cytoplasmic diffusion coefficient is significantly lower than in the nucleus. The same was true for G2 phase cytoplasmic and nuclear diffusivities. The diffusion coefficient in both the nucleus and cytoplasm reduces significantly as the cell cycle progresses and our label-free measurements agree with estimates of spatially variable intracellular diffusivity over similar time scales using quantum dots (*59*).

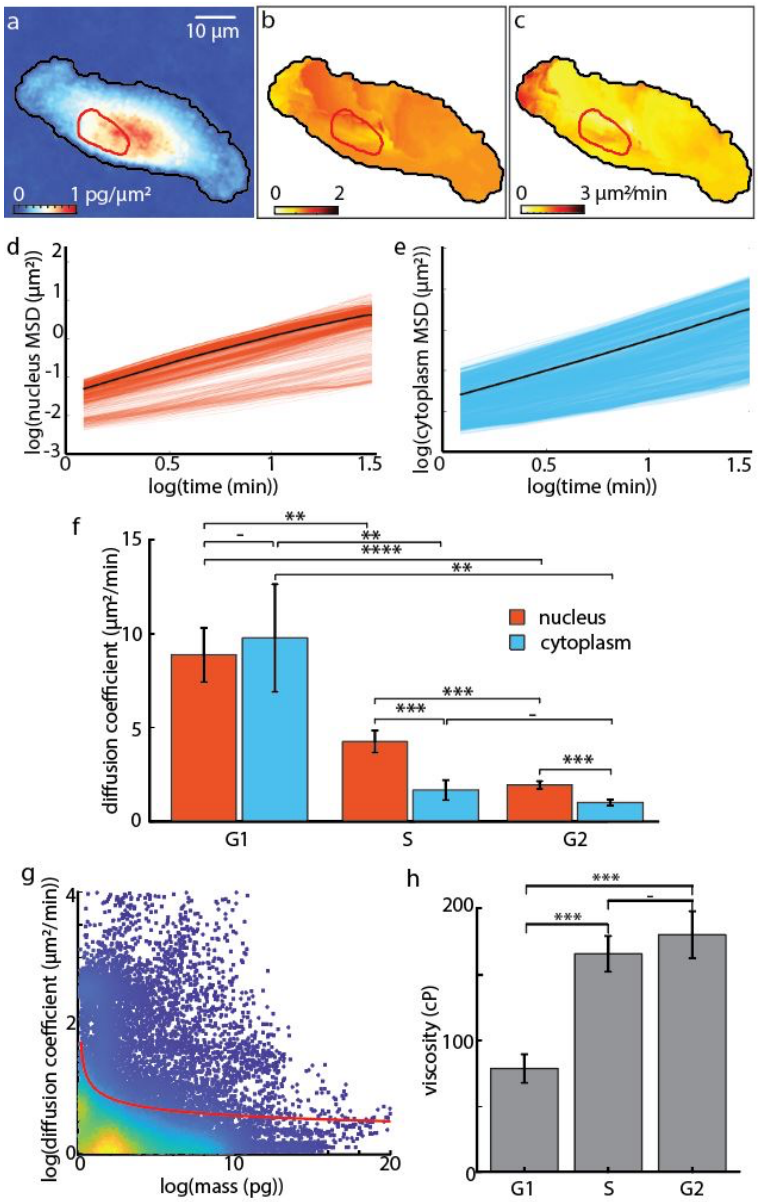


**Figure 5. Mean squared displacement (MSD) analysis shows reduced diffusion coefficient in RPE cells with cell cycle progression.** (a) QPI image of individual RPE cell with red nuclear and black cytoplasmic boundary shown. (b) Anomalous constant distribution within

the RPE cell from (a). (c) Diffusion coefficient distribution within the RPE cell from (a). (d) Logarithm of MSD vs time lag of intracellular volumes in the nucleus of the RPE cell in (a). The black line shows the mean of all nuclear volumes. Black line shows the mean of all cytoplasmic volumes. (f) Nuclear and cytoplasmic diffusion coefficients in RPE cells over the cell cycle from $n$ = 119 cells. Error bars show standard error of the mean. (g) Diffusion coefficient versus mass for all regions tracked inside RPE cells. Red line shows best fit power law which has a scaling exponent of -0.233. (h) Live cell viscosity measured from combination of QPV measured diffusion coefficient and the effective particle size from QPI power spectra of corresponding cells. ** $p < 0.01$, *** $p < 1\text{x}10^{-3}$, **** $p < 1\text{x}10^{-4}$.

As a method that tracks mass of intracellular components, we can apply QPI to determine the dependence of the measured diffusivity of each control volume on its mass. We find a moderate fit to a power law (R = 0.2) with a scaling exponent of -0.233 (**figure 5h**). This is close to the expected scaling of $D \sim m^{-1/3}$ that would be predicted from Stokes-Einstein, assuming mass scales with the cube of effective particle size, but with significant deviation at the level of individual control volumes.

Finally, we applied QPV as a method to estimate the effective intracellular viscosity from cell cycle dependent measurements of diffusivity (**figure S12a**). We estimated the effective size of particles tracked by QPV from the power spectra of QPI images (**figure 3a**), limited to particles that are within the window size used for QPV. This yields a roughly constant effective particle size through the cell cycle (**figure S12b**). From these measurements, we estimate the effective intracellular viscosity using the Stokes-Einstein relationship to detect an increase with progression through the cell cycle (**figure 5h**). The magnitude of this estimate from label-free QPV is consistent with previous measurements based on molecular rotors or FRET probes (*60-62*).

## DISCUSSION

We developed QPV to measure intracellular velocity from QPI (**figure 1**). We found that, for the typical distribution of features in QPI images of cells, SSD has better performance than other commonly used image registration techniques such as MI and NCC, at a wider range of displacements than OFR (**figure 2**). Thus, we based QPV on the SSD image registration method. Theoretical modeling of the sources of error in QPV agrees well with error characterizations using fixed cells (**figure 3**) and reveals that window size, particle size variation, the optical resolution limit, and random diffusion in cells are key factors that limit velocity measurement precision. We then applied QPV to measure mass transport within cells throughout the cell cycle. The intracellular velocity results from QPV showed more directed motion of mass in the nucleus and more random deformations unrelated to overall cell movement in the cytoplasm (**figure 4**). We applied MSD analysis of QPV derived subcellular trajectories to measure intracellular effective diffusivity and viscosity through the cell cycle (**figure 5**).

Our model of error contributions to QPV points towards possible improvements. One key insight is that the particle size distribution is critical in determining the accuracy of QPV. This suggests that a high-pass filtering scheme may improve accuracy of QPV by reducing the effective particle size. However, this would come at the loss of applicability to tracking whole cell displacements, as the resulting velocity fields would be for aa subset of intracellular particles. We also note that this is the inverse of OFR, which shows improved tracking of large displacements using Gaussian blurring, a low-pass filtering method (*56*). We also note that, though Brownian motion was found to be a key limit to the accuracy of velocity estimation for previous applications of PIV to microscopy data to measure flow within microchannels (*63, 64*), we found the influence of Brownian motion to have a small impact on QPV. We estimate an impact of <3% for the smallest particle sizes imaged and negligible impact for the largest particles tracked.

As a method to measure intracellular viscosity, QPV gives estimates that are consistent with fluorescent methods that rely on FRET or molecular rotors (*60-62*). QPV is, therefore, a simpler alternative for measurements of intracellular viscosity. We note that, though we based our method on quadri-wave lateral shearing interferometry (*36*), there are a large number of alternative methods for QPI (*31-34, 36*), any of which should be amenable to QPV. Our

viscometry results, in particular, show an increase in viscosity with cell cycle progression, which may be due to macromolecular crowding accompanying growth (*65*).

QPV has a number of advantages over alternative approaches for studying mass transport within cells. Unlike many other label-free methods, QPV automatically tracks intracellular features based on PIV. Additionally, as a label-free method, QPV avoids issues with phototoxicity, photobleaching, or label dilution over time, while still giving results for intracellular diffusivity and viscosity that are comparable in magnitude to methods requiring labels. Another major advantage of QPV is that it uses the same analysis for both nucleus and cytoplasm, allowing direct comparisons between these two compartments that are difficult to label consistently with other approaches. Overall, this work suggests that QPV is a valuable tool to study intracellular transport and biophysics.

## MATERIALS AND METHODS

### Microscopy

We performed QPI with an Olympus IX83 inverted microscope (Olympus Corporation, Japan) in brightfield with a 100X, 1.3 numerical aperture oil-immersion objective, and 1.2X magnifier to match the Nyquist criteria with a Phasics SID4-4MP (Phasics, France) camera. 120 ms exposure with red LED illumination (623 nm, DC2200, Thorlabs, USA) was used for QPI image acquisition. We used MATLAB (Mathworks, USA) for automated image acquisition. We connected the illumination sources, Retiga camera and stage with MicroManager open-source microscopy software (*66*). The Olympus IX83 microscope (Olympus corporation, Japan) and Phasics camera were connected directly through MATLAB. QPI images were captured every 1 minute and fluorescence images every 30 minutes at 30 imaging positions in every dataset. A flipping mirror arrangement (IX3-RSPCA, Olympus Corporation. USA) enabled alternate fluorescent and QPI. X-Cite 120LED light source (Excelitas technologies, USA) and Retiga R1 camera (Cairn research Ltd, UK) at 300 ms exposure were used for the fluorescence, with an Olympus U-FBNA filter cube for green mAG fluorophore and Semrock mCherry-B-000 filter cube (IDEX health & science, USA) for imaging the red mKO2 fluorophore. Uniform 37°C and 5% $CO_2$ conditions were maintained using an Okolab stage-top incubator (Okolab, Italy) and custom-built objective heating collar, temperature controlled by Thorlabs temperature controller (Thorlabs, USA). For live cell imaging, cells were plated in Ibidi μ-high treated dishes at 30% confluence. Four sets of 30 live cells were imaged every for 8 hours for every imaging session.

### Cell culture

Cell culture procedures complied with the University of Utah BSL-2 guidelines. MCF7 (mammary epithelium) cell lines donated by Welm lab (HCI, Utah) were cultured in Dulbecco's modified eagle's medium (DMEM) (Gibco™ 11330057, Thermo Fisher Scientific, USA) with 10% fetal bovine serum (FBS) (Corning™ 35015CV, Fisher Scientific, USA). mKO2-hCdt1 and mAG-hGem tagged FUCCI expressing RPE-1 cells from Edgar lab (HCI, Utah), prepared by Yiqin Ma, were cultured in Gibco DMEM with 10% FBS and 5% Penicillin-Streptomycin. Penicillin-Streptomycin was removed while imaging the cells. Cells were split 1 to 6 to 1 to 3 ratio at confluence less than 80% at a frequency based on their growth rate.

**Cell FUCCI tagging**

RPE cells donated by the lab of Bruce Edgar (University of Utah) were received FUCCI tagged with mAG-hGem and mKO2-hCDt1. Cells express the mKO2 tag on Cdt1 in the nucleus during G1 phase (red nucleus), added mAG tag on Geminin in the nucleus during S phase (yellow nucleus due to combination of red mKO2 and green mAG) and the loss of mKO2 with the onset of G2 phase (green nucleus). The fluorescent image of the FUCCI tagged nuclei captured every 30 minutes was segmented using the k-mean algorithm (available as a built-in function in MATLAB) and overlapped with the QPI image.

**Mycoplasma testing**

We DAPI (Fisher-NC9677247) stained fixed cells, grown 80 to 90 % confluent, after permeabilizing the nuclei using methanol at 4ºC, to test for mycoplasma contamination. The DAPI stained cells were imaged using a Retiga R1 camera at 500 ms exposure time and Olympus U-FUNA filter cube, illuminated by X-Cite 120LED. We checked the presence of DAPI stained puncta outside the nucleus as an indicator for mycoplasma contamination.

**Initial processing of QPI data**

The Phasics SID4BIO camera for QPI uses a modified Hartmann mask diffraction grating to compute the phase gradient in two orthogonal directions which were converted to phase measurements using the Phasics Matlab SDK (Phasics, France). Phase shift was converted to dry mass using an assumed specific refractive increment of 0.18 $\mu m^3$/pg for cell material (*31*). The phase shift of light ($\phi$) expressed as an optical path length is directly related to the dry mass ($m$) at a given pixel through the specific refractive increment (α) (*67*) as:

$$m = \frac{1}{\alpha} \int \phi dA \tag{1}$$

where $A$ is the area of each pixel of the phase shift image. QPI images were then background corrected by fourth order polynomial curve fitting to regions in the phase image outside of cells.

**Fixed cell imaging**

RPE and MCF7 cells were plated in Ibidi μ-high treated dish at 40% confluence. Cells were fixed by removing cell culture media, washing with PBS and incubating in 4% paraformaldehyde

(PFA) at 37ºC for 10 minutes. The PFA was further removed, cells washed with PBS, refilled with fresh PBS and sealed and stored until imaging. During imaging, the dish was heated to 37ºC on Okolab stage-top incubator 20 minutes prior to imaging to avoid condensation. Cells were imaged at each 0.05 µm step stage translation in the vertical direction.

**Image registration**

*Sum of squared differences (SSD)*

SSD was then performed on overlapping discretized interrogation windows of 15 by 15 pixels, spaced by 1 pixel, in the background corrected QPI image. The SSD of two image regions was computed as:

$$SSD(i,j) = \sum_{i=0}^{M} \sum_{j=0}^{N} \left(f(i,j) - g(i+u, j+v)\right)^2 \tag{2}$$

where $f$ and $g$ are the two interrogation windows from successive images to be matched using SSD with $i$ and $j$ the location of pixels comprising the image, $M$ and $N$ are the width and length of the image in pixels and $u$ and $v$ are the displacement introduced at each iteration of the SSD calculation.

Gaussian fitting on 3 by 3 pixel localized lowest pixel neighborhood in SSD plane was used for sub-pixel displacement localization. Spurious velocities were removed using a conditional median filter, thus retaining the original values of subcellular velocity computed. Processing was performed using computational resources allocated by the Center for High Performance Computing (CHPC) at the University of Utah. Code is available on GitHub (https://github.com/ZangleLab).

*Normalized cross correlation (NCC)*

NCC between interrogation windows was measured using the MATLAB function *normxcorr2*. The displacement of the highest pixel in the correlation plane from the center pixel was used to compute the displacement of the each interrogation window.

*Optical flow reconstruction (OFR)*

OFR developed by Lucas and Kanade (*68*) measures the transport of intensity profile in images, given by

$$\frac{\Delta I}{\Delta t} = \frac{I(t + \Delta t) - I(t)}{\Delta t} = -v.\nabla I \quad (3)$$

Here $I(t+\Delta t)$ and $I(t)$ are intensity of images time $\Delta t$ apart, in our case 1 minute. We used the code available from (*15*) for OFR displacement calculation. The *BlurSize* parameter for blurring image using Gaussian blurring before OFR in code was set to 1. The *BlurStd* parameter was set to 1,2,5,8 and 12 for understanding impact of Gaussian blurring (figure S4 c and d).

*Mutual Information (MI)*

MI was computed using a method implemented in Matlab that extracts mutual information from the joint histogram and joint entropy of the registered images that was adapted to perform mutual information (MI) image registration calculation on sliding interrogation windows inside grayscale QPI images (*69*).

**Calculation of measurement error**

The error of displacement magnitude ($E_{mag}$) was calculated as:

$$E_{mag} = \frac{(D_{real} - D_{measured})}{D_{real}} \times 100\ \% \quad (4)$$

where $D_{real}$ is the actual magnitude of displacement introduced by movement of stage, and $D_{measured}$ is the average measured displacement magnitude.

Direction error ($E_{dir}$) was computed as the angle between the computed and actual displacement vector:

$$E_{dir} = \theta_{real} - \theta_{measured} \quad (5)$$

$\theta_{real}$ is the actual angle of displacement introduced by stage and $\theta_{measured}$ is the average angle measured by image registration method.

**QPV error model**

Power spectra of the cell images was azimuthally averaged to convert power density image to 2-dimensional plot of power density vs frequency.

We estimated the optical diffraction limit as:

$$Diffraction\ limit = \frac{\lambda}{NA}$$

(6)

where $\lambda$ is the wavelength of light and $NA$ is the numerical aperture of the objective used for imaging, assuming that the illumination NA = 0 to generate a spatially coherent plane wave for QPI (*36*). The code for constructing the particle size dependent error model is also available on GitHub (https://github.com/ZangleLab).

**Deformation velocity**

The whole cell velocity was computed based on tracking segmented cell centroids. The cell nucleus was segmented from cytoplasm using k-means segmentation algorithm on FUCCI fluorescence images. Cytoplasm and nucleus mask were used to separate subcellular 3-minute displacement tracks in corresponding regions and used to compute cytoplasm and nuclear velocities separately. The average cell centroid velocity was subtracted from all intracellular velocities and averaged in cytoplasm and nucleus to compute the deformation velocity of cytoplasm and nucleus.

**MSD analysis and viscosity**

Relation between MSD and time lag ($\tau$) is given by

$$<MSD> = 4D\tau^{\alpha} \tag{7}$$

D is the diffusion coefficient and $\alpha$ is the anomalous constant. The proportionality constant is 4D as the tracking is two-dimensional.

Viscosity is calculated from Stokes Einstein relation, $\mu = \frac{kT}{3\pi D d_p}$, where the diffusion coefficient ($D$) is obtained from MSD analysis, $k$ is the Boltzmann constant, and $T$ is the temperature. The effective particle size ($d_p$) is obtained from power spectrum of QPI image of the cell, weighting the particle size by the power spectrum density, within the limit of particle sizes visible by the interrogation window size.

**Statistics**

Welch's two-tailed t test with unequal variances was used to calculate the significance of differences between experimental groups. Error bars are reported as the standard error of the mean based on the number of cells in each test group.

## REFERENCES


1. W. Palm, C. B. Thompson, Nutrient acquisition strategies of mammalian cells. *Nature* **546**, 234-242 (2017).
2. H. Lodish, A. Berk, C. A. Kaiser, M. Krieger, A. Bretscher, H. Ploegh, A. Amon, K. C. Martin, Molecular Cell Biology. *W. H. Freeman and Company* **8th edition**, (2016).
3. A. J. Ridley, M. A. Schwartz, K. Burridge, R. A. Firtel, M. H. Ginsberg, G. Borisy, J. T. Parsons, A. R. Horwitz, Cell Migration: Integrating Signals from Front to Back. *Science* **302**, 1704 (2003).
4. M. Kuwahara, F. Marumo, Diseases caused by disorders of membrane transport: an overview. *Nihon rinsho. Japanese journal of clinical medicine* **54**, 581-585 (1996).
5. M. Kodiha, U. Stochaj, Nuclear transport: a switch for the oxidative stress-signaling circuit? *J Signal Transduct* **2012**, 208650 (2012).
6. E. V. Sviderskaya, E. Jazrawi, S. A. Baldwin, C. C. Widnell, C. A. Pasternak, Cellular Stress Causes Accumulation of the Glucose Transporter at the Surface of Cells Independently of their Insulin Sensitivity. *The Journal of Membrane Biology* **149**, 133-140 (1996).
7. E. F. Koslover, C. K. Chan, J. A. Theriot, Cytoplasmic Flow and Mixing Due to Deformation of Motile Cells. *Biophys J* **113**, 2077-2087 (2017).
8. S. Seirin Lee, T. Shibata, Self-organization and advective transport in the cell polarity formation for asymmetric cell division. *Journal of theoretical biology* **382**, 1-14 (2015).
9. H. H. Chung, S. D. Bellefeuille, H. N. Miller, T. R. Gaborski, Extended live-tracking and quantitative characterization of wound healing and cell migration with SiR-Hoechst. *Exp Cell Res* **373**, 198-210 (2018).
10. M. Liebel, J. Ortega Arroyo, V. S. Beltrán, J. Osmond, A. Jo, H. Lee, R. Quidant, N. F. van Hulst, 3D tracking of extracellular vesicles by holographic fluorescence imaging. *Science Advances* **6**, eabc2508 (2020).
11. F. Progatzky, M. J. Dallman, C. Lo Celso, From seeing to believing: labelling strategies for in vivo cell-tracking experiments. *Interface Focus* **3**, 20130001 (2013).
12. M. P. Sheetz, J. A. Spudich, Movement of myosin-coated fluorescent beads on actin cables in vitro. *Nature* **303**, 31-35 (1983).
13. J. Sankaran, T. Wohland, Fluorescence strategies for mapping cell membrane dynamics and structures. *APL Bioeng* **4**, 020901 (2020).
14. A. Boquet-Pujadas, T. Lecomte, M. Manich, R. Thibeaux, E. Labruyere, N. Guillen, J. C. Olivo-Marin, A. C. Dufour, BioFlow: a non-invasive, image-based method to measure speed, pressure and forces inside living cells. *Sci Rep* **7**, 9178 (2017).
15. D. K. Vig, A. E. Hamby, C. W. Wolgemuth, On the Quantification of Cellular Velocity Fields. *Biophys J* **110**, 1469-1475 (2016).
16. H. A. Shaban, R. Barth, L. Recoules, K. Bystricky, Hi-D: nanoscale mapping of nuclear dynamics in single living cells. *Genome Biol* **21**, 95 (2020).
17. S. J. Kron, J. A. Spudich, Fluorescent actin filaments move on myosin fixed to a glass surface. *Proceedings of the National Academy of Sciences* **83**, 6272 (1986).
18. E. C. Jensen, Types of Imaging, Part 2: An Overview of Fluorescence Microscopy. *The Anatomical Record* **295**, 1621-1627 (2012).
19. R. Dixit, R. Cyr, Cell damage and reactive oxygen species production induced by fluorescence microscopy: effect on mitosis and guidelines for non-invasive fluorescence microscopy. *Plant J* **36**, 280-290 (2003).

20. A. M. Valm, R. Oldenbourg, G. G. Borisy, Multiplexed Spectral Imaging of 120 Different Fluorescent Labels. *PLoS One* **11**, e0158495 (2016).
21. T. Vicar, J. Balvan, J. Jaros, F. Jug, R. Kolar, M. Masarik, J. Gumulec, Cell segmentation methods for label-free contrast microscopy: review and comprehensive comparison. *BMC Bioinformatics* **20**, 360 (2019).
22. D. House, M. L. Walker, W. Zheng, J. Y. Wong, M. Betke, in *2009 IEEE Computer Society Conference on Computer Vision and Pattern Recognition Workshops*. (2009), pp. 186-193.
23. K. Li, E. D. Miller, M. Chen, T. Kanade, L. E. Weiss, P. G. Campbell, Cell population tracking and lineage construction with spatiotemporal context. *Med Image Anal* **12**, 546-566 (2008).
24. M. Feith, T. Vičar, J. Gumulec, M. Raudenská, A. Gjörloff Wingren, M. Masařík, J. Balvan, Quantitative Phase Dynamics of Cancer Cell Populations Affected by Blue Light. *Applied Sciences* **10**, (2020).
25. R. Kasprowicz, R. Suman, P. O'Toole, Characterising live cell behaviour: Traditional label-free and quantitative phase imaging approaches. *Int J Biochem Cell Biol* **84**, 89-95 (2017).
26. S. A. Kollimada, A. H. Kulkarni, A. Ravan, N. Gundiah, Advancing Edge Speeds of Epithelial Monolayers Depend on Their Initial Confining Geometry. *PLoS One* **11**, e0153471 (2016).
27. W. Zhang, Y. Xu, G. Chen, K. Wang, W. Shan, Y. Chen, Dynamic single-vesicle tracking of cell-bound membrane vesicles on resting, activated, and cytoskeleton-disrupted cells. *Biochim Biophys Acta Biomembr* **1861**, 26-33 (2019).
28. A. R. Chaphalkar, Y. K. Jawale, D. Khatri, C. A. Athale, Quantifying Intracellular Particle Flows by DIC Object Tracking. *Biophys J*, (2021).
29. X. Nan, E. O. Potma, X. S. Xie, Nonperturbative chemical imaging of organelle transport in living cells with coherent anti-stokes Raman scattering microscopy. *Biophys J* **91**, 728-735 (2006).
30. R. Barer, Interference microscopy and mass determination. *Nature* **169**, 366-367 (1952).
31. T. A. Zangle, M. A. Teitell, Live-cell mass profiling: an emerging approach in quantitative biophysics. *Nat Methods* **11**, 1221-1228 (2014).
32. P. Muller, G. Cojoc, J. Guck, DryMass: handling and analyzing quantitative phase microscopy images of spherical, cell-sized objects. *BMC Bioinformatics* **21**, 226 (2020).
33. Z. Wang, L. Millet, M. Mir, H. Ding, S. Unarunotai, J. Rogers, M. U. Gillette, G. Popescu, Spatial light interference microscopy (SLIM). *Opt Express* **19**, 1016-1026 (2011).
34. L. Tian, L. Waller, Quantitative differential phase contrast imaging in an LED array microscope. *Opt Express* **23**, 11394-11403 (2015).
35. B. C. Platt, R. Shack, History and principles of Shack-Hartmann wavefront sensing. *J Refract Surg* **17**, S573-577 (2001).
36. P. Bon, G. Maucort, B. Wattellier, S. Monneret, Quadriwave lateral shearing interferometry for quantitative phase microscopy of living cells. *Opt Express* **17**, 13080-13094 (2009).
37. A. F. Brown, G. A. Dunn, Microinterferometry of the movement of dry matter in fibroblasts. *J Cell Sci* **92 ( Pt 3)**, 379-389 (1989).

38. J. Reed, J. J. Troke, J. Schmit, S. Han, M. A. Teitell, J. K. Gimzewski, Live cell interferometry reveals cellular dynamism during force propagation. *ACS Nano* **2**, 841-846 (2008).
39. R. Wang, Z. Wang, J. Leigh, N. Sobh, L. Millet, M. U. Gillette, A. J. Levine, G. Popescu, One-dimensional deterministic transport in neurons measured by dispersion-relation phase spectroscopy. *J Phys Condens Matter* **23**, 374107 (2011).
40. T. A. Zangle, J. Chun, J. Zhang, J. Reed, M. A. Teitell, Quantification of biomass and cell motion in human pluripotent stem cell colonies. *Biophys J* **105**, 593-601 (2013).
41. T. L. Nguyen, E. R. Polanco, A. N. Patananan, T. A. Zangle, M. A. Teitell, Cell viscoelasticity is linked to fluctuations in cell biomass distributions. *Sci Rep* **10**, 7403 (2020).
42. W. J. Eldridge, Z. A. Steelman, B. Loomis, A. Wax, Optical Phase Measurements of Disorder Strength Link Microstructure to Cell Stiffness. *Biophys. J.* **112**, 692-702 (2017).
43. Z. Wang, L. Millet, V. Chan, H. Ding, M. U. Gillette, R. Bashir, G. Popescu, Label-free intracellular transport measured by spatial light interference microscopy. *J Biomed Opt* **16**, 026019 (2011).
44. P. A. Sandoz, C. Tremblay, F. G. van der Goot, M. Frechin, Image-based analysis of living mammalian cells using label-free 3D refractive index maps reveals new organelle dynamics and dry mass flux. *PLoS Biol.* **17**, e3000553 (2019).
45. Y. Park, M. Diez-Silva, G. Popescu, G. Lykotrafitis, W. Choi, M. S. Feld, S. Suresh, Refractive index maps and membrane dynamics of human red blood cells parasitized by Plasmodium falciparum. *Proceedings of the National Academy of Sciences* **105**, 13730-13735 (2008).
46. L. Ma, G. Rajshekhar, R. Wang, B. Bhaduri, S. Sridharan, M. Mir, A. Chakraborty, R. Iyer, S. Prasanth, L. Millet, M. U. Gillette, G. Popescu, Phase correlation imaging of unlabeled cell dynamics. *Sci Rep* **6**, 32702 (2016).
47. A. Kumar, A. Maitra, M. Sumit, S. Ramaswamy, G. V. Shivashankar, Actomyosin contractility rotates the cell nucleus. *Sci Rep* **4**, 3781 (2014).
48. J. P. W. Pluim, J. B. A. Maintz, M. A. Viergever, Mutual-information-based registration of medical images: a survey. *IEEE Transactions on Medical Imaging* **22**, 986-1004 (2003).
49. J. N. Sarvaiya, S. Patnaik, S. Bombaywala, in *2009 International Conference on Advances in Computing, Control, and Telecommunication Technologies*. (2009), pp. 819-822.
50. M. B. Hisham, S. N. Yaakob, R. A. A. Raof, A. B. A. Nazren, N. M. Wafi, in *2015 IEEE Student Conference on Research and Development (SCOReD)*. (2015), pp. 100-104.
51. L. Petitjean, M. Reffay, E. Grasland-Mongrain, M. Poujade, B. Ladoux, A. Buguin, P. Silberzan, Velocity fields in a collectively migrating epithelium. *Biophys. J.* **98**, 1790-1800 (2010).
52. J. Sankaran, M. Manna, L. Guo, R. Kraut, T. Wohland, Diffusion, transport, and cell membrane organization investigated by imaging fluorescence cross-correlation spectroscopy. *Biophys J* **97**, 2630-2639 (2009).
53. D. G. Lowe, Distinctive Image Features from Scale-Invariant Keypoints. *International Journal of Computer Vision* **60**, 91-110 (2004).

54. T. Netsch, P. Rosch, A. v. Muiswinkel, J. Weese, in *Proceedings Eighth IEEE International Conference on Computer Vision. ICCV 2001*. (2001), vol. 1, pp. 718-725 vol.711.
55. P. Bon, G. Maucort, B. Wattellier, S. Monneret, Quadriwave lateral shearing interferometry for quantitative phase microscopy of living cells. *Opt Express* **17**, 13080-13094 (2009).
56. N. Sharmin, R. Brad, Optimal Filter Estimation for Lucas-Kanade Optical Flow. *Sensors* **12**, 12694-12709 (2012).
57. N. Zielke, B. A. Edgar, FUCCI sensors: powerful new tools for analysis of cell proliferation. *Wiley Interdiscip Rev Dev Biol* **4**, 469-487 (2015).
58. K. Szczepanski, K. Kwapiszewska, R. Holyst, Stability of cytoplasmic nanoviscosity during cell cycle of HeLa cells synchronized with Aphidicolin. *Sci Rep* **9**, 16486 (2019).
59. H. Li, S. X. Dou, Y. R. Liu, W. Li, P. Xie, W. C. Wang, P. Y. Wang, Mapping intracellular diffusion distribution using single quantum dot tracking: compartmentalized diffusion defined by endoplasmic reticulum. *J Am Chem Soc* **137**, 436-444 (2015).
60. X. Peng, Z. Yang, J. Wang, J. Fan, Y. He, F. Song, B. Wang, S. Sun, J. Qu, J. Qi, M. Yan, Fluorescence ratiometry and fluorescence lifetime imaging: using a single molecular sensor for dual mode imaging of cellular viscosity. *J Am Chem Soc* **133**, 6626-6635 (2011).
61. T. Liu, X. Liu, D. R. Spring, X. Qian, J. Cui, Z. Xu, Quantitatively mapping cellular viscosity with detailed organelle information via a designed PET fluorescent probe. *Sci Rep* **4**, 5418 (2014).
62. M. K. Kuimova, G. Yahioglu, J. A. Levitt, K. Suhling, Molecular Rotor Measures Viscosity of Live Cells via Fluorescence Lifetime Imaging. *Journal of the American Chemical Society* **130**, 6672-6673 (2008).
63. J. G. Santiago, S. T. Wereley, C. D. Meinhart, D. J. Beebe, R. J. Adrian, A particle image velocimetry system for microfluidics. *Exp Fluids* **25**, 316-319 (1998).
64. C. D. Meinhart, S. T. Wereley, J. G. Santiago, A PIV algorithm for estimating time-averaged velocity fields. *J Fluid Eng-T Asme* **122**, 285-289 (2000).
65. G. Nettesheim, I. Nabti, C. U. Murade, G. R. Jaffe, S. J. King, G. T. Shubeita, Macromolecular crowding acts as a physical regulator of intracellular transport. *Nature Physics* **16**, 1144-1151 (2020).
66. A. Edelstein, N. Amodaj, K. Hoover, R. Vale, N. Stuurman, Computer Control of Microscopes Using µManager. *Current Protocols in Molecular Biology* **92**, 14.20.11-14.20.17 (2010).
67. R. Barer, S. Joseph, Refractometry of Living Cells. *Quarterly Journal of Microscopical Science* **s3-95**, 399 (1954).
68. B. D. Lucas, T. Kanade, paper presented at the Proceedings of the 7th international joint conference on Artificial intelligence - Volume 2, Vancouver, BC, Canada, 1981.
69. H. xb, *a function with the simplest form to calculate the mutual information (https://www.mathworks.com/matlabcentral/fileexchange/42165-a-function-with-the-simplest-form-to-calculate-the-mutual-information)* (MATLAB Central File Exchange. Retrieved March 11, 2019).

**ACKNOWLEDGMENTS**

This work was supported by the University of Utah and NIH K25CA157940. We thank Dr. Bruce Edgar's lab, Dr. Yiqin Ma at the Huntsman Cancer Institute, University of Utah for donation of FUCCI tagged RPE cells. We also thank Dr. Alana Welm's lab at Huntsman Cancer Institute, University of Utah for donation of MCF7 cells. Finally, the support and resources from the Center for High Performance Computing at the University of Utah are gratefully acknowledged.